In/Bi-based Direct- and Indirect-Gap Hybrid Double-Perovskite-Derived 1D Halides with Near-Unity Quantum Yield via Sb³⁺ Doping

Ruiqian Li, Yifan Zhou, Xuanyu Zhang, Jiawei Lin, Jian Chen, Congcong Chen, Xin Pan, Pan Wang, Rui Chen, Jun Yin,* and Lingling Mao*

Read Online

ACCESS | Metrics & More | Article Recommendations | Supporting Information

ABSTRACT: The hybrid halide double-perovskite family is a highly diverse system that allows a wide range of property tunings via structural variations. Using organic components instead of small *A*-site cations to reduce the dimensionality of the structure and doping metal cations can modulate their structure and improve the optoelectronic performance. Here, by introducing an organic cationic ligand morpholine (Mor), we report on a new family of double-perovskite-derived halides $(Mor)_2ABX_6$ (A = Na, K; B = In, Bi; X = Cl, Br) with several unique types of one-dimensional (1D) structures constituted by $[AX_4O_2]$ and $[BX_6]$ octahedron units. These materials are nonemissive at room temperature, while with an Sb³⁺-doping strategy, the photoluminescence can be drastically enhanced. For $(Mor)_2KInX_6$, their quantum efficiencies are improved to near unity via Sb³⁺ doping. Meanwhile, for $(Mor)_2KBiX_6$, the photoluminescence improvement from Sb³⁺ doping is negligible. With density functional theory calculations, $(Mor)_2KInBr_6$ and $(Mor)_2KBiBr_6$ have been identified to have direct- and indirect- band gap, respectively. This work expands a new material space for organic−inorganic hybrid double-perovskite-derived materials and provides insights into tuning their optical properties.
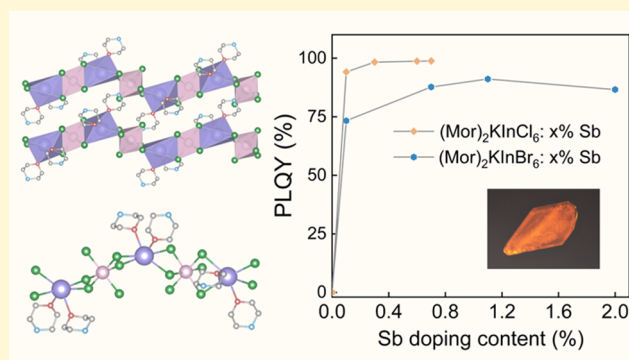
INTRODUCTION

Halide perovskites are great candidates for optoelectronics because of their high absorption coefficients, easily tunable energy gaps, high carrier mobility, and excellent defect tolerance.[1−6] These superior properties led to promising applications in solar cells, photodetectors, light-emitting diodes (LEDs), and a wide range of optoelectronic applications.[7−11] The strategy of using monovalent and trivalent metal cations instead of Pb²⁺ to form double perovskites effectively avoids lead toxicity issues.[12,13] In(III) as one of the 3+ metal options has the advantages of tunable light emission, environmentally friendly characteristics, and resistance to oxidation. For instance, In(III)-based double perovskites such as $Cs_2NaInCl_6$ have been explored and exhibit practical application for X-ray detectors.[14−16] Despite that these materials have large Stokes shifts, self-trapped excitons (STEs) broad emission, and structural diversity brought by the combination of different metal elements, the presence of parity-forbidden transition and nonradiative composite processes in double perovskites lead to undesirable photoluminescence quantum yield (PLQY).[17,18]

Compared with other main group metals, antimony-based halides have been widely reported to have high PLQYs. For example, $(MePPh_3)_2SbCl_5$, $(PPN)_2SbCl_5$ (PPN^+ = bis-(triphenylphosphoranylidene)-ammonium), $(Me_3BzN)_2SbCl_5$ $((Me_3BzN)^+$ = trimethylbenzyl ammonium), and $(Et_3BzN)_2SbCl_5$ $((Et_3BzN)^+$ = triethylbenzyl ammonium) all have near-unity PLQY.[19−21] Furthermore, with dynamic lone pairs, Sb³⁺ has been widely used as an efficient dopant to enhance the photoluminescence (PL) efficiency.[22−25] $Cs_2InCl_5·H_2O$ with 5% Sb³⁺ demonstrated a strong electron−phonon coupling, which led to the formation of STE emission with a near-unity PLQY.[26] In another example, Sb³⁺-doped $(C_{22}H_{25}P)_2MnCl_4$ exhibited excellent thermal stability while having a high PLQY of 84%.[27] Through doping Sb³⁺, $(DFPD)_2KInBr_6$ (DFPD = 4,4-difluoropiperidinium) achieved highly efficient warm-white PL emission.[28]

In addition, the low-dimensional structure can enable adapting to a much more distorted octahedral coordination geometry and facilitate the radiative recombination of bound excitons.[29−32] Using organic components instead of small *A*-site cations in the double perovskite can reduce the dimensionality of the structure to modulate its structure and provide additional structural flexibility that cannot be achieved
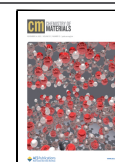
with a simple double-perovskite motif.[33−36] For instance, butylammonium (BA) cations were incorporated into the framework of three-dimensional (3D) halide double-perovskite $Cs_2AgBiBr_6$ to generate $BA_4AgBiBr_8$ accompanied by indirect-to-direct band gap transition.[37] Other low-dimensional double-perovskite derivatives include $(MA)_2AgInBr_6$, where face-sharing $[AgBr_6]$ and $[InBr_6]^{3−}$ octahedra are connected alternately to form one-dimensional (1D) chains.[38]

Here, by introducing an organic component morpholine (Mor) as the cationic ligand, we have obtained a series of 1D double-perovskite-derived compounds with the general formula $(Mor)_2ABX_6$ (A = Na, K; B = In, Bi; X = Cl, Br). The oxygen in Mor and the halogens are coordinated to K and help in stabilization of the bimetallic units. The PLQY of the In-based materials has been significantly enhanced by doping Sb^{3+} up to near unity, while the Bi-based materials, even though structurally analogous, are difficult to dope and only show a little improvement. With density functional theory (DFT) calculations, we further reveal that the In-based materials are direct-gap semiconductors, while the Bi-based materials are indirect-gap, which explains their intrinsic differences. Our work demonstrates a new design perspective regarding the double-perovskite-derived family and illustrates the fundamental aspects for effective property tuning.

EXPERIMENTAL METHODS

Synthesis. Potassium bromide (99.19%), sodium chloride (99.9%), antimony(III) oxide (99.2%), bismuth(III) oxide (99.5%), indium(III) oxide (99.5%), and morpholine (99%) were purchased from Bide Pharmatech Ltd. Hydrochloric acid (analytical reagent, 40%) and hydrogen bromide (analytical reagent, 40%) were purchased from Shanghai Macklin Biochemical Co., Ltd. All reagents and materials were directly used without further treatment.

$(Mor)_2ABX_6$ was synthesized via solution methods. B_2O_3 (1 mmol) and NaCl/KBr (1 mmol) were dissolved in 5 mL of HX, and 2 mmol of Mor was added dropwise to the previous mixture under heating and stirring until the solution became homogeneous. Colorless or pale yellow needlelike crystals of $(Mor)_2KBX_6$ precipitated after the reaction mixture was cooled to ambient temperature. For preparing $(Mor)_2KInX_6$, 1% Sb, In_2O_3 (0.99 mmol), Sb_2O_3 (0.01 mmol), and KBr (1 mmol) were dissolved in 5 mL of HX, and 2 mmol Mor was added dropwise to the previous mixture. By removing the resultant solution after heating and stirring until homogeneous, colorless/pale yellow plate-like crystals can be obtained at room temperature. For preparing $(Mor)_2KInX_6$, 3% Sb, In_2O_3 (0.97 mmol), Sb_2O_3 (0.03 mmol), and KBr (1 mmol) were dissolved in 5 mL of HX, and 2 mmol Mor was added dropwise to the previous mixture. By removing the resultant solution after heating and stirring until homogeneous, colorless/pale yellow plate-like crystals can be obtained at room temperature. For preparing $(Mor)_2ABX_6$, 5% Sb, B_2O_3 (0.95 mmol), Sb_2O_3 (0.05 mmol), and NaCl/KBr (1 mmol) were dissolved in 5 mL of HX, and 2 mmol Mor was added dropwise to the previous mixture. By removing the resultant solution after heating and stirring until homogeneous, colorless/pale yellow plate-like crystals could be obtained at room temperature. For preparing $(Mor)_2KInX_6$: 8% Sb, In_2O_3 (0.92 mmol), Sb_2O_3 (0.08 mmol), and KBr (1 mmol) were dissolved in 5 mL of HX, and 2 mmol Mor was added dropwise to the previous mixture. By removing the resultant solution after heating and stirring until homogeneous, colorless/pale yellow plate-like crystals can be obtained at room temperature.

Single-Crystal X-ray Diffraction (SCXRD). Full sphere data were collected for single crystals of $(Mor)_2ABX_6$ (A = Na, K; B = In, Bi; X = Cl, Br) collected using a Bruker D8 VENTURE diffractometer with Ga/Mo Kα radiation at 298 K, with the integration and reduction of crystal data carried out by the Bruker APEX3 software. Crystal structures were solved using Olex2 program.[39]

Powder X-ray Diffraction (PXRD). Powder X-ray diffraction patterns were collected for powder samples using a SmartLab X-ray Diffractometer with Cu Kα radiation at room temperature.

UV−vis Spectroscopy. The ultraviolet−visible (UV−vis) spectra, using the UV-3600i Plus spectrophotometer with $BaSO_4$ as the reference material, were collected in the wavelength range of 200−1000 nm at room temperature. The band gaps are converted using the Kubelka−Munk equation $\alpha/S = (1 − R)^2/2R$, where α, S, and R represent the absorption coefficient, scattering coefficient, and absolute reflectance, respectively.

Steady-State, Time-Resolved, and Temperature-Dependent PL. The PL spectra were obtained with a HORIBA FluoroMax+ instrument. The excitation wavelength was 320 nm for Sb^{3+}-doped $(Mor)_2NaInCl_6$, 325 nm for Sb^{3+}-doped $(Mor)_2KInCl_6$, 360 nm for $(Mor)_2KBiBr_6$, and 365 nm for $(Mor)_2KInBr_6$, Sb^{3+}-doped $(Mor)_2KInBr_6$, and Sb^{3+}-doped $(Mor)_2NaInBr_6$. The PLQYs were measured at room temperature using the integrating sphere on a Xi Pu Guang Dian XP-EQE-Adv instrument with excitation at 365 nm. Temperature-dependent PL experiments were performed in a cryostat cooled with liquid nitrogen. A thermocouple connected to a temperature controller was used to monitor and control the temperature during measurements. All samples were excited with MDL-III laser, and the corresponding PL spectra were collected using a NOVA spectrometer through the OLYMPUS confocal microscope.

Inductively Coupled Plasma Mass Spectroscopy (ICP-MS). ICP-MS measurements were conducted using an Agilent 7700X ICP-MS spectrometer.

Density Functional Theory (DFT) Calculations. DFT calculations were carried out using the projector-augmented wave (PAW) method as implemented in the Vienna Ab initio Simulation Package (VASP) code. The generalized gradient approximation (GGA) level with the Perdew−Burke−Ernzerhof (PBE) functional was used. The van der Waals (vdW) interactions were also included in the calculations using the zero-damping method of Grimme (DFT-D3). A uniform grid of 4 × 2 × 1 k-mesh in the Brillouin zone was employed to optimize the crystal structures of $(Mor)_2KInBr_6$ and $(Mor)_2KBiBr_6$. The plane-wave basis set cutoff of the wave functions was set at 450 eV. The atomic positions of both crystal structures were fully relaxed until the forces on each atom were less than 0.01 eV/Å. The band structures, projected density of states (PDOS), and electronic charge densities were calculated at the GGA/PBE+vdW level with spin−orbit coupling (SOC) effects.

RESULTS AND DISCUSSION

Crystal Structure Analysis. Morpholine was chosen as the organic cationic ligand because of its structure containing an oxygen atom for coordination with the alkali metal, and the nitrogen on the ring could be protonated for charge balance. The sp^3 oxygen atoms in organic cationic ligands, such as ethanolammonium (EA) and methyl-2-hydroxyethylammonium (MEA), have been shown to participate in the constitution of the metal halide octahedra and generate large distortions.[40] Single-crystal X-ray diffraction (SCXRD) analyses revealed that the $(Mor)_2KBX_6$ (X = Cl, Br) are isostructural and crystallize in the monoclinic space group $C2/c$, whereas $(Mor)_2NaInCl_6$ and $(Mor)_2NaInBr_6$ crystallize in the monoclinic space group $P2/c$ and $P2_1/c$, respectively (detailed crystallographic data are given in Tables S1−S3). The phase purity was confirmed via powder X-ray diffraction (PXRD) for the same features of the samples and simulation results (Figures S1−S3). We have previously reported the structure of $(Mor)_2KBiBr_6$,[40] whereas the other structures are all new and are first reported here. These compounds have unique 1D structures constituted by $[KX_4O_2]$ and $[BX_6]$ octahedron units. In $(Mor)_2KInCl_6$, K coordinates with four Cl and two O from Mor, and In coordinates with six Cl, forming the alternating 1D chains in two edge-sharing ways (Figure

1a,c,e). The Mor cation, while balancing the charge, forms a $[KCl_4O_2]$ octahedron in coordination with K. In addition, Bi
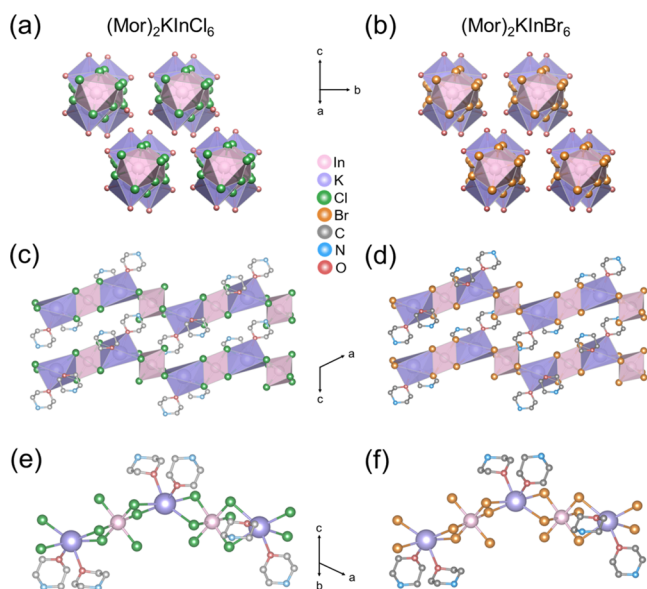
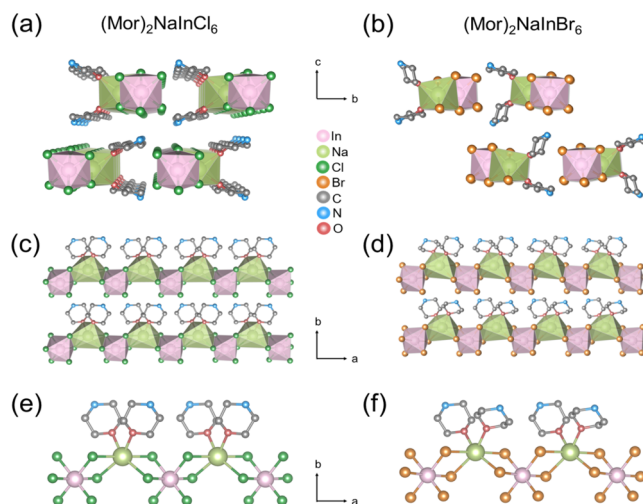**Figure 1.** Crystal structure of (a) $(Mor)_2KInCl_6$ along the direction perpendicular to the 1D chains, (b) $(Mor)_2KInBr_6$ along the direction perpendicular to the 1D chains. (c) $(Mor)_2KInCl_6$ and (d) $(Mor)_2KInBr_6$ viewing from the *b*-axis, showing the alternating polyhedra of different metal centers. Basic building units were (e) $(Mor)_2KInCl_6$ and (f) $(Mor)_2KInBr_6$. Hydrogens are omitted for clarity.

was chosen to replace In to explore the structural diversity. We have obtained isostructural compounds with $[KX_4O_2]$ and $[BiX_6]$ forming the alternating 1D chains in edge-sharing ways as expected (Figure 2a−d). It means that the central atom of
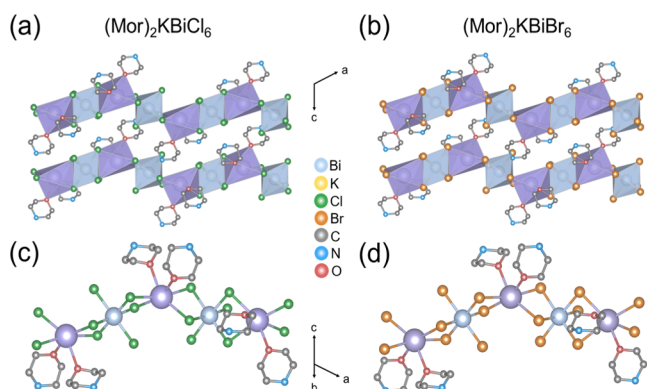
Figure 2. Crystal structures of (a) $(Mor)_2KBiCl_6$ and (b) $(Mor)_2KBiBr_6$ on viewing from the *b*-axis. Basic building units were (c) $(Mor)_2KBiCl_6$ and (d) $(Mor)_2KBiBr_6$. Hydrogens are omitted for clarity.

the $[BX_6]$ octahedron is not the decisive factor in the formation of this structure. Then we replace K with Na to explore the effect of *A*-site metal cations on the structures. For $(Mor)_2NaInX_6$, however, different from the K analogues, $[NaX_4O_2]$ is linked with $[InX_6]$ through only one edge-sharing mode, where the organic cations all orientate upward along the *b*-axis (Figure 3a−f). For all of the above compounds, replacing Cl with Br, we still get isomorphic compounds,

Figure 3. Crystal structures of (a) $(Mor)_2NaInCl_6$ and (b) $(Mor)_2NaInBr_6$ on viewing from the *a*-axis. Structures of (c) $(Mor)_2NaInCl_6$ and (d) $(Mor)_2NaInBr_6$ on viewing from the *c*-axis, where the cationic ligand is situated on one side of the chain. Basic building units are (e) $(Mor)_2NaInCl_6$ and (f) $(Mor)_2NaInBr_6$. Hydrogens are omitted for clarity.

which indicates that replacing the halogen would not change the structure of this series of compounds. Furthermore, we tried to replace K with other alkali metals but failed to obtain the target compounds. This probably could be attributed to the ionic radius of the alkali metal ions and the affinity toward the coordination, where only appropriate-sized metal cations can lead to the formation of the desired structure.

Optical Properties. We have measured the optical band gaps of $(Mor)_2ABX_6$ by diffuse reflectance spectroscopy on solid powder samples. The optical band gaps, determined by extrapolating the absorbing edge to the linear part, are 4.5 eV for $(Mor)_2KInCl_6$, 3.6 eV for $(Mor)_2KInBr_6$, 3.3 eV for $(Mor)_2KBiCl_6$, 3.0 eV for $(Mor)_2KBiBr_6$, 4.9 eV for $(Mor)_2NaInCl_6$, and 3.7 eV for $(Mor)_2NaInBr_6$ (Figure 4a−c and Table 1). These band gaps are comparable with other reported materials, such as $(PMA)_3InBr_6$ (3.78 eV), $(PBA)_4InBr_7 \cdot H_2O$ (4.05 eV, $(PBA)^+ = C_6H_5(CH_2)_4NH_3^+$), $(PBA)_4BiBr_7 \cdot H_2O$ (3.52 eV), and $[(ArNH_3)_3(BiBr_6)]$ (2.92 eV, Ar = 2,6-diisopropylphenyl).[41−43] Comparing $(Mor)_2NaInBr_6$ vs $(Mor)_2KInBr_6$, they have very similar band gaps, which indicate that the *A*-site metal and the structural connectivity have little effect on the band gaps.[40] However, in the case of $(Mor)_2NaInCl_6$ vs $(Mor)_2KInCl_6$, the difference in the band gap is pronounced (~0.5 eV), which hints that the chlorides are more sensitive in terms of structure and composition. For the other sets of comparisons, the band gaps of the derivatives with different *B*-site metals or halides differ significantly. In-based compounds have much larger band gaps than Bi-based isostructural ones. By replacing the Cl in $(Mor)_2AInCl_6$ with Br, the band gap was decreased by about 1 eV, which is commonly seen for the hybrid metal halides.[44] For $(Mor)_2KBiX_6$, the band gap difference between the compounds formed with Cl and Br is 0.3 eV, which is much less significant than that in $(Mor)_2AInX_6$.

Although the pristine materials are almost nonemissive, we collected the PL data for $(Mor)_2KInX_6$. The PL spectrum of $(Mor)_2KInX_6$ is mainly dominated by a broadband extremely weak orange emission peaking at 660 nm for $(Mor)_2KInCl_6$ and 700 nm for $(Mor)_2KInBr_6$ (Figure S5). The broadband

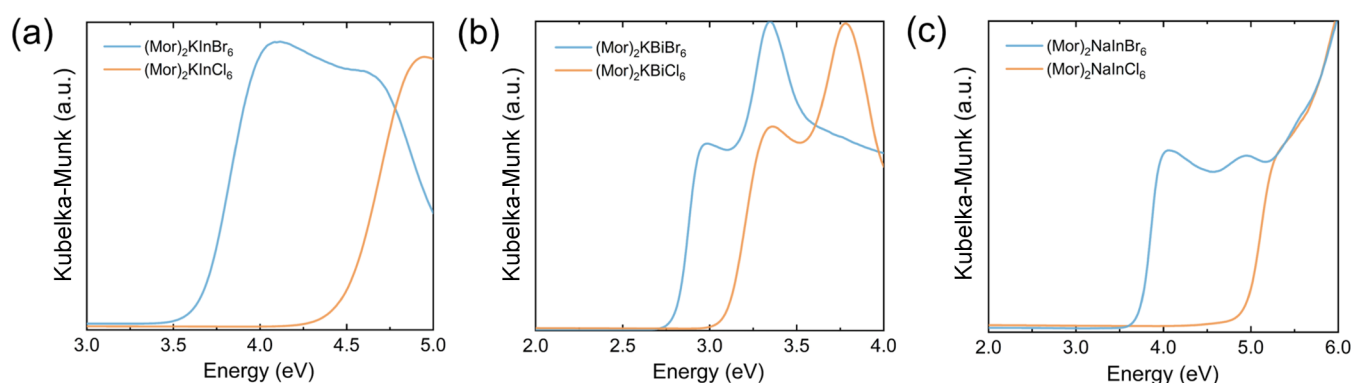**Figure 4.** UV−vis absorption spectra of (a) $(Mor)_2KInX_6$, (b) $(Mor)_2KBiX_6$, and (c) $(Mor)_2NaInX_6$ (X = Cl, Br).

Table 1. Comparison of the Optical Band Gaps of $(Mor)_2ABX_6$

compounds	band gap (eV)
$(Mor)_2KBiCl_6$	3.3
$(Mor)_2KBiBr_6$	3.0
$(Mor)_2KInCl_6$	4.5
$(Mor)_2KInBr_6$	3.6
$(Mor)_2NaInCl_6$	4.9
$(Mor)_2NaInBr_6$	3.7

emission and a large Stokes shift resemble those previously reported for STE emissions.[45,46]

PLQY Enhancement in Sb³⁺-Doped $(Mor)_2ABX_6$. Because of its similar size and charge, Sb^{3+} has been chosen as the dopant to enhance the PL performance. The doping concentration is noted as the percentage of Sb^{3+} to the total amount of In^{3+} and Sb^{3+}, which is kept at 1 mmol. The actual introduced mole ratios (x) of Sb to (In + Sb) in Sb³⁺-doped $(Mor)_2KBX_6$ samples were identified by ICP-MS measurement (detailed data are given in Tables S4−S6). For Sb³⁺-doped $(Mor)_2NaInX_6$, we denote it as $(Mor)_2NaInX_6$: 5%; here 5% refers to the proportion of Sb^{3+} to In^{3+} and Sb^{3+} in the feed ratio. The relevant characterization results for $(Mor)_2AB_{1-x}Sb_xX_6$ are listed here. The PXRD patterns of Sb³⁺-doped $(Mor)_2ABX_6$ are identical to the undoped ones, indicating that the Sb³⁺-doped products are single phases like the pristine samples (Figures 5a,b, S8, and S12). In addition, magnified images of the PXRD patterns show that the peaks are slightly shifted to low angles in $(Mor)_2KInX_6$ (Figure S11).

For $(Mor)_2KInX_6$ and $(Mor)_2KBiBr_6$, under UV lamp irradiation at room temperature, orange light is emitted after doping Sb^{3+} (Figures 5c and S5). The emission peak of the Sb³⁺-doped $(Mor)_2KInCl_6$ center at 660 nm and the highest PL intensity are excited with an λ_{ex} of 325 nm (Figure S5b). Their PL emission follows the same mechanism because their excitation and emission peaks differ only in intensity but not in position. As previously reported, ns^2-based metal cations such as Sb^{3+}, possessing a lone pair that can be emitted from the radiative recombination, have the ground state ($^1S_0$) and their first excited state generally split into single state ($^1P_1$) and triplet state (^3P_n).[47] Meanwhile, the lifetime of the triplet $^1S_0 \rightarrow {}^3P_n$ radiative recombination with partially forbidden transition (several microseconds) is usually longer than that of the singlet $^1S_0 \rightarrow {}^1P_1$ (several nanoseconds). The lifetime of the emission peak is determined as 4.03 μs for Sb³⁺-doped $(Mor)_2KInCl_6$ at 280 K. Therefore, the emission can be assigned to the triplet $^1S_0 \rightarrow {}^3P_n$. Likewise, as shown in Figures 5c and S5d, the Sb³⁺-doped $(Mor)_2KInBr_6$ shows orange light emission centered at 700 nm. $(Mor)_2KBiBr_6$ emits a faint orange light with a weak emission at 710 nm after doping Sb^{3+} (Figure S10). However, for $(Mor)_2KBiCl_6$, the doping strategy did not improve the luminescence properties. Figure S14a shows the excitation and emission spectra of $(Mor)_2NaInCl_6$: 5% Sb, with green light emission at 545 nm. Under the optimal excitation wavelength of 365 nm, $(Mor)_2NaInBr_6$: 5% Sb exhibits a broadband yellow light emission center at 580 nm (Figure S14b). Replacing K with Na of smaller size causes changes in structure and space group. Their structural differences result in distinct emission colors. A similar case
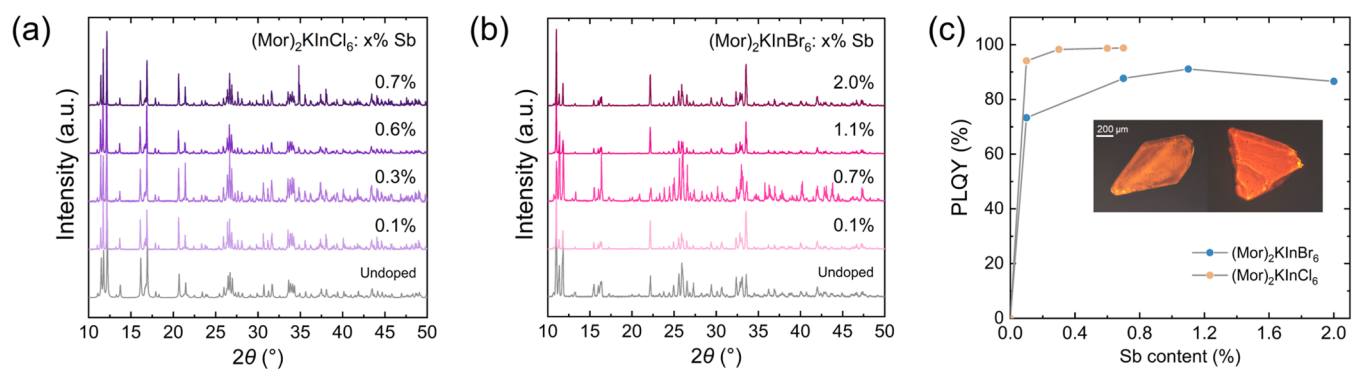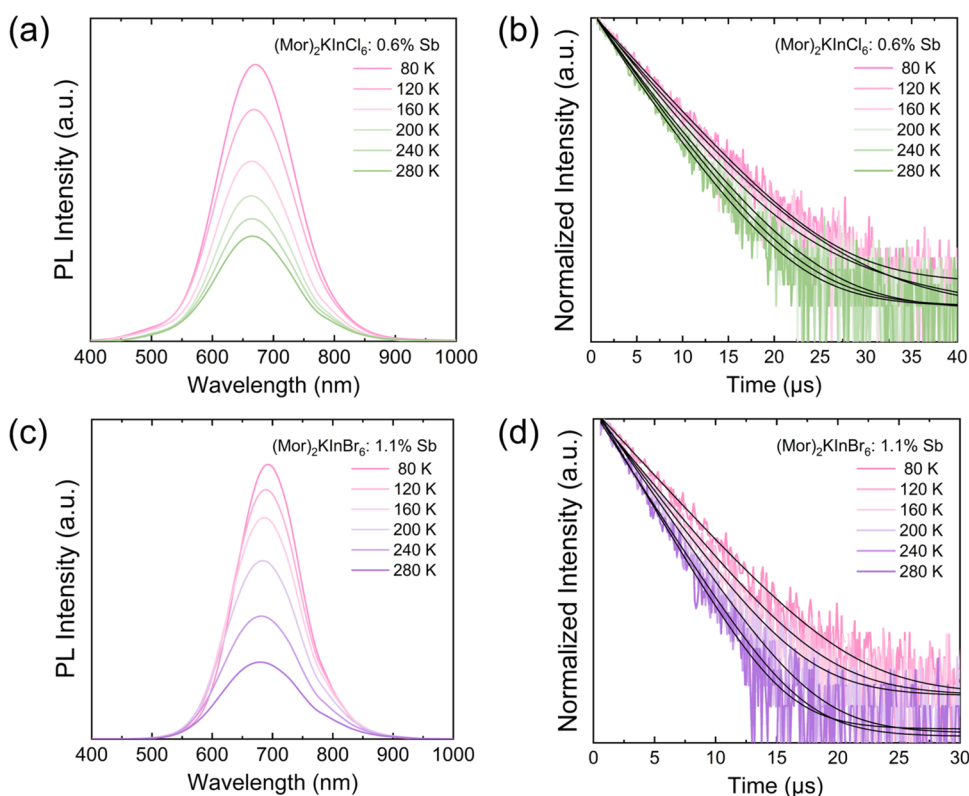

Figure 5. PXRD of Sb³⁺-doped (a) $(Mor)_2KInCl_6$ and (b) $(Mor)_2KInBr_6$ with varying Sb concentrations determined by ICP-MS. (c) Dependence of PLQY on Sb^{3+} doping concentration for the $(Mor)_2KInX_6$ series (X = Cl, Br). Inset images are optical microscopic pictures of $(Mor)_2KIn_{0.994}Sb_{0.006}Cl_6$ (left) and $(Mor)_2KIn_{0.989}Sb_{0.011}Br_6$ (right) under UV excitation.

Figure 6. (a) Temperature-dependent steady-state PL spectra of $(Mor)_2KInCl_6$: 0.6% Sb. (b) Temperature-dependent PL decay spectra of $(Mor)_2KInCl_6$: 0.6% Sb. (c) Temperature-dependent steady-state PL spectra of $(Mor)_2KInBr_6$: 1.1%. (d) Temperature-dependent time-resolved PL decay spectra of $(Mor)_2KInBr_6$: 1.1%.

can be found in a previous report, using Na to replace K, where $Cs_2NaInCl_6$:5%Sb showed a blue-shift trend in PL emission peak.[48]

As expected, their PLQYs are greatly enhanced with this approach. The PLQY of Sb^{3+}-doped $(Mor)_2KInCl_6$ is raised to 98.8%, and the highest PLQY for Sb^{3+}-doped $(Mor)_2KInBr_6$ rises to 91.1% (Figure 5c). The maximum PLQY of Sb^{3+}-doped $(Mor)_2KBiBr_6$ can reach only 0.2% at the same doping concentration, while the PLQY of $(Mor)_2KBiCl_6$ is ~0% after doping. The PLQYs for $(Mor)_2NaInCl_6$: 5% Sb and $(Mor)_2NaInBr_6$: 5% Sb increase to 48.2 and 3.6%, respectively. The lifetime of $(Mor)_2KInCl_6$: 0.6% Sb decreases from 5.19 to 4.03 μs and the lifetime of $(Mor)_2KInBr_6$: 1.1% Sb decreases from 3.85 to 2.51 μs (Figure 6a−d and Table S7) with increasing temperature from 80 to 280 K. The fwhm broadens at high temperatures, implying the increase of electronic coupling with acoustic phonons. To evaluate the strength of interaction, we obtained Huang−Rhys factor S by the following equation

$$\text{FWHM}(T) = 2.36\sqrt{S}\, h\omega_{phone}\sqrt{\coth\frac{h\omega_{phone}}{2k_BT}}$$

where $h\omega_{phone}$ is the phonon frequency and k_B is the Boltzmann constant. The S factor was determined to be 16.1 (Figure S15), which is lower than that of $Cs_3Sb_2I_9$ ($S = 42$).[49] In order to deeply explore the electron−phonon coupling interaction, Γ_{op} was fitted as 184.3 meV by Toyokawa equation

$$\Gamma(T) = \Gamma_0 + \Gamma_{op}/(e^{h\omega_{op}/Kk_BT} - 1)$$

where Γ_0 is the intrinsic line width at an absolute temperature of 0 K, Γ_{op} is the electron-optical phonon coupling energy, and $h\omega_{op}$ is the longitudinal optical phonon energy (Figure S16). These results indicate that there is a relatively strong electron−phonon coupling interaction in Sb^{3+}-doped $(Mor)_2KInBr_6$.

DFT Calculations. To investigate the underlying factors influencing the divergence in optical properties within In/Bi-based compounds and to acquire a better understanding of their luminescence mechanisms, density functional theory (DFT) calculations on $(Mor)_2KInBr_6$ and $(Mor)_2KBiBr_6$ were carried out at GGA/PBE level with van der Waals (vdW) interactions and spin−orbit coupling (SOC) effects. As shown in Figure 7a,d, $(Mor)_2KInBr_6$ exhibits a direct band gap while $(Mor)_2KBiBr_6$ displays an indirect band gap. This alignment corresponds with the observation that $(Mor)_2KInBr_6$ shows better optical performances (i.e., higher PL intensity and PLQY). The compounds with direct band gap exhibit absorption and recombination exclusively governed by photons, resulting in high absorption coefficients and accelerated carrier recombination. Conversely, in compounds with indirect band gap, both photons and phonons play roles in absorption and recombination, leading to poor optical performances.[17] This elucidates the superior optical properties (i.e., much higher PLQY) exhibited by $(Mor)_2KInBr_6$ compared to $(Mor)_2KBiBr_6$. The calculated band gap at the GGA/PBE level with vdW+SOC is 2.69 eV for $(Mor)_2KInBr_6$ and 2.59 eV for $(Mor)_2KBiBr_6$; both are smaller than experimental values. However, both the calculated and experimental values align in the trend of variation, where the band gap of $(Mor)_2KInBr_6$ is larger than $(Mor)_2KBiBr_6$.
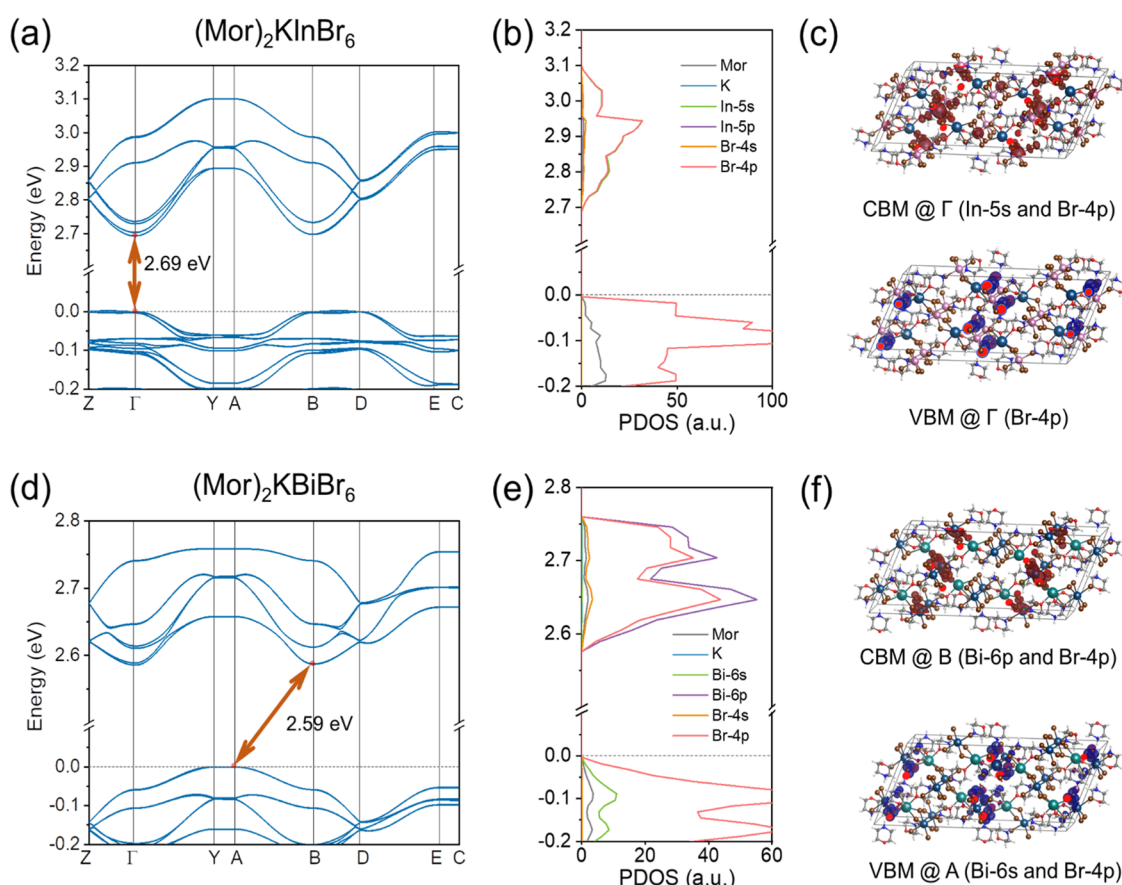
Figure 7. Density functional theory (DFT) calculations at the GGA/PBE + vdW + SOC level. Calculated band structures for (a) $(Mor)_2KInBr_6$ and (d) $(Mor)_2KBiBr_6$. Projected density of states (PDOS) of (b) $(Mor)_2KInBr_6$ and (e) $(Mor)_2KBiBr_6$. Electronic charge densities for the valence band maximum (VBM) and conduction band minimum (CBM) of (c) $(Mor)_2KInBr_6$ and (f) $(Mor)_2KBiBr_6$.

The PDOS shows that in $(Mor)_2KInBr_6$, the valence band maximum (VBM) originates from the 5s orbitals of In and the 4p orbitals of Br, while the conduction band minimum (CBM) is derived from the 4p orbitals of Br (Figure 7b,c). The VBM and CBM, both located at the Γ-point, are mainly determined by the $[InBr_6]^{3-}$ octahedra, which is similar to other In-based organic−inorganic hybrids, such as $(DFPD)_4InBr_7$ and $(DFPD)_2KInBr_6$.[28] In $(Mor)_2KBiBr_6$, the VBM originates from the 6p orbitals of Bi and the 4p orbitals of Br, while the CBM consists of the 4p orbitals of Br and the 6s orbitals of Bi (Figure 7e,f). Likewise, the band edges of $(Mor)_2KBiBr_6$ predominantly originate from the inorganic part.

CONCLUSIONS

Five new hybrid double-perovskite-derived 1D halides $(Mor)_2ABX_6$ (A = Na, K; B = In, Bi; X = Cl, Br) have been synthesized and characterized in this work. These materials have unique structures with alternating metal halide centers, and the different size of the metal induces variations of connectivity modes. The triplet $^1S_0 \rightarrow {}^3P_n$ radiative recombination originated from the dopant Sb^{3+} enables drastic PLQY enhancement for these materials. The PLQY of $(Mor)_2KInX_6$ can be improved from 0% to near unity by Sb^{3+} doping. For the $(Mor)_2KBiX_6$, Sb^{3+} doping hardly improves the PLQYs, which could be due to the intrinsic indirect band nature. Via DFT calculations, $(Mor)_2KInBr_6$ and $(Mor)_2KBiBr_6$ have been demonstrated to have direct and indirect band gap, respectively. Our work provides new insights into the design and property enhancement of the double-perovskite-derived materials.

ASSOCIATED CONTENT

Supporting Information

The Supporting Information is available free of charge at https://pubs.acs.org/doi/10.1021/acs.chemmater.3c02183.

> Additional characterization including UV−vis spectrum; PL spectrum; and crystallographic details (PDF)

Accession Codes

Crystallographic cif. files have been deposited as CCDC number 2272077−2272079, 2285452, and 2285453.

AUTHOR INFORMATION

Corresponding Authors

Jun Yin − *Department of Applied Physics, The Hong Kong Polytechnic University, Hung Hom, Kowloon, Hong Kong SAR 999077, China;* ⬡ orcid.org/0000-0002-1749-1120; Email: jun.yin@polyu.edu.hk

Lingling Mao − *Department of Chemistry, Southern University of Science and Technology, Shenzhen 518055, China;* ⬡ orcid.org/0000-0003-3166-8559; Email: maoll@sustech.edu.cn

Authors

Ruiqian Li − *Department of Chemistry, Southern University of Science and Technology, Shenzhen 518055, China*

Yifan Zhou − *Department of Applied Physics, The Hong Kong Polytechnic University, Hung Hom, Kowloon, Hong Kong SAR 999077, China*

Xuanyu Zhang − *Department of Electrical and Electronic Engineering, Southern University of Science and Technology, Shenzhen 518055, China*

Jiawei Lin − *Department of Chemistry, Southern University of Science and Technology, Shenzhen 518055, China*

Jian Chen − *Department of Chemistry, Southern University of Science and Technology, Shenzhen 518055, China*

Congcong Chen − *Department of Chemistry, Southern University of Science and Technology, Shenzhen 518055, China;* ⬤ orcid.org/0000-0003-1016-8731

Xin Pan − *Department of Chemistry, Southern University of Science and Technology, Shenzhen 518055, China*

Pan Wang − *Department of Chemistry, Southern University of Science and Technology, Shenzhen 518055, China*

Rui Chen − *Department of Electrical and Electronic Engineering, Southern University of Science and Technology, Shenzhen 518055, China;* ⬤ orcid.org/0000-0002-0445-7847

Complete contact information is available at:
https://pubs.acs.org/10.1021/acs.chemmater.3c02183

Notes
The authors declare no competing financial interest.

REFERENCES

(1) Fakharuddin, A.; Gangishetty, M. K.; Abdi-Jalebi, M.; Chin, S.-H.; bin Mohd Yusoff, A. R.; Congreve, D. N.; Tress, W.; Deschler, F.; Vasilopoulou, M.; Bolink, H. J. Perovskite light-emitting diodes. *Nat. Electron.* **2022**, *5* (4), 203−216. DOI: 10.1038/s41928-022-00745-7.

(2) Jena, A. K.; Kulkarni, A.; Miyasaka, T. Halide Perovskite Photovoltaics: Background, Status, and Future Prospects. *Chem. Rev.* **2019**, *119* (5), 3036−3103.

(3) Jia, P.; Lu, M.; Sun, S.; Gao, Y.; Wang, R.; Zhao, X.; Sun, G.; Colvin, V. L.; Yu, W. W. Recent Advances in Flexible Perovskite Light-Emitting Diodes. *Adv. Mater. Interfaces* **2021**, *8* (17), No. 2100441.

(4) Snaith, H. J. Present status and future prospects of perovskite photovoltaics. *Nat. Mater.* **2018**, *17* (5), 372−376.

(5) Stranks, S. D.; Snaith, H. J. Metal-halide perovskites for photovoltaic and light-emitting devices. *Nat. Nanotechnol.* **2015**, *10* (5), 391−402.

(6) Zhao, C.; Zhang, D.; Qin, C. Perovskite Light-Emitting Diodes. *CCS Chem.* **2020**, *2* (4), 859−869.

(7) Cao, Y.; Wang, N.; Tian, H.; Guo, J.; Wei, Y.; Chen, H.; Miao, Y.; Zou, W.; Pan, K.; He, Y.; et al. Perovskite light-emitting diodes based on spontaneously formed submicrometre-scale structures. *Nature* **2018**, *562* (7726), 249−253.

(8) Gao, L.; Zhang, F.; Xiao, C.; Chen, X.; Larson, B. W.; Berry, J. J.; Zhu, K. Improving Charge Transport via Intermediate-Controlled Crystal Growth in 2D Perovskite Solar Cells. *Adv. Funct. Mater.* **2019**, *29* (47), No. 1901652.

(9) Zhao, B.; Bai, S.; Kim, V.; Lamboll, R.; Shivanna, R.; Auras, F.; Richter, J. M.; Yang, L.; Dai, L.; Alsari, M.; et al. High-efficiency perovskite−polymer bulk heterostructure light-emitting diodes. *Nat. Photonics* **2018**, *12* (12), 783−789.

(10) Zhu, H.; Liu, A.; Noh, Y.-Y. Perovskite transistors clean up their act. *Nat. Electron.* **2020**, *3* (11), 662−663.

(11) Zhu, H.; Liu, A.; Shim, K. I.; Hong, J.; Han, J. W.; Noh, Y. Y. High-Performance and Reliable Lead-Free Layered-Perovskite Transistors. *Adv. Mater.* **2020**, *32* (31), No. 2002717.

(12) Martín-García, B.; Spirito, D.; Lin, M. L.; Leng, Y. C.; Artyukhin, S.; Tan, P. H.; Krahne, R. Low-Frequency Phonon Modes in Layered Silver-Bismuth Double Perovskites: Symmetry, Polarity, and Relation to Phase Transitions. *Adv. Opt. Mater.* **2022**, *10* (14), No. 2200240. DOI: 10.1002/adom.202200240.

(13) Muscarella, L. A.; Hutter, E. M. Halide Double-Perovskite Semiconductors beyond Photovoltaics. *ACS Energy Lett.* **2022**, *7* (6), 2128−2135.

(14) Li, Z.; Song, G.; Li, Y.; Wang, L.; Zhou, T.; Lin, Z.; Xie, R.-J. Realizing Tunable White Light Emission in Lead-Free Indium(III) Bromine Hybrid Single Crystals through Antimony(III) Cation Doping. *J. Phys. Chem. Lett.* **2020**, *11* (23), 10164−10172.

(15) Locardi, F.; Cirignano, M.; Baranov, D.; Dang, Z.; Prato, M.; Drago, F.; Ferretti, M.; Pinchetti, V.; Fanciulli, M.; Brovelli, S.; et al. Colloidal Synthesis of Double Perovskite $Cs_2AgInCl_6$ and Mn-Doped $Cs_2AgInCl_6$ Nanocrystals. *J. Am. Chem. Soc.* **2018**, *140* (40), 12989−12995.

(16) Peng, Y.; Li, L.; Ji, C.; Wu, Z.; Wang, S.; Liu, X.; Yao, Y.; Luo, J. Tailored Synthesis of an Unprecedented Pb−Mn Heterometallic Halide Hybrid with Enhanced Emission. *J. Am. Chem. Soc.* **2019**, *141* (31), 12197−12201.

(17) Luo, J.; Wang, X.; Li, S.; Liu, J.; Guo, Y.; Niu, G.; Yao, L.; Fu, Y.; Gao, L.; Dong, Q.; et al. Efficient and stable emission of warm-white light from lead-free halide double perovskites. *Nature* **2018**, *563* (7732), 541−545.

(18) Yang, B.; Mao, X.; Hong, F.; Meng, W.; Tang, Y.; Xia, X.; Yang, S.; Deng, W.; Han, K. Lead-Free Direct Band Gap Double-Perovskite Nanocrystals with Bright Dual-Color Emission. *J. Am. Chem. Soc.* **2018**, *140* (49), 17001−17006.

(19) He, Q.; Zhou, C.; Xu, L.; Lee, S.; Lin, X.; Neu, J.; Worku, M.; Chaaban, M.; Ma, B. Highly Stable Organic Antimony Halide Crystals for X-ray Scintillation. *ACS Mater. Lett.* **2020**, *2* (6), 633−638.

(20) Li, J. L.; Sang, Y. F.; Xu, L. J.; Lu, H. Y.; Wang, J. Y.; Chen, Z. N. Highly Efficient Light-Emitting Diodes Based on an Organic Antimony(III) Halide Hybrid. *Angew. Chem., Int. Ed.* **2021**, *61* (6), No. e202113450. DOI: 10.1002/anie.202113450.

(21) Sun, C.; Deng, Z.; Li, Z.; Chen, Z.; Zhang, X.; Chen, J.; Lu, H.; Canepa, P.; Chen, R.; Mao, L. Achieving Near-unity Photoluminescence Quantum Yields in Organic-Inorganic Hybrid Antimony (III) Chlorides with the $[SbCl_5]$ Geometry. *Angew. Chem., Int. Ed.* **2023**, *62* (10), No. e202216720. DOI: 10.1002/anie.202216720.

(22) Laurita, G.; Fabini, D. H.; Stoumpos, C. C.; Kanatzidis, M. G.; Seshadri, R. Chemical tuning of dynamic cation off-centering in the cubic phases of hybrid tin and lead halide perovskites. *Chem. Sci.* **2017**, *8* (8), 5628−5635.

(23) Laurita, G.; Seshadri, R. Chemistry, Structure, and Function of Lone Pairs in Extended Solids. *Acc. Chem. Res.* **2022**, *55* (7), 1004−1014.

(24) McCall, K. M.; Morad, V.; Benin, B. M.; Kovalenko, M. V. Efficient Lone-Pair-Driven Luminescence: Structure−Property Relationships in Emissive $5s^2$ Metal Halides. *ACS Mater. Lett.* **2020**, *2* (9), 1218−1232.

(25) Xiao, Z.; Song, Z.; Yan, Y. From Lead Halide Perovskites to Lead-Free Metal Halide Perovskites and Perovskite Derivatives. *Adv. Mater.* **2019**, *31* (47), No. 1803792.

(26) Jing, Y.; Liu, Y.; Jiang, X.; Molokeev, M. S.; Lin, Z.; Xia, Z. Sb^{3+} Dopant and Halogen Substitution Triggered Highly Efficient and

Tunable Emission in Lead-Free Metal Halide Single Crystals. *Chem. Mater.* **2020**, *32* (12), 5327−5334.

(27) Li, C.; Luo, Z.; Liu, Y.; Wei, Y.; He, X.; Chen, Z.; Zhang, L.; Chen, Y.; Wang, W.; Liu, Y.; et al. Self-Trapped Exciton Emission with High Thermal Stability in Antimony-Doped Hybrid Manganese Chloride. *Adv. Opt. Mater.* **2022**, *10* (12), No. 2102746.

(28) Bai, T.; Wang, X.; Wang, Z.; Ji, S.; Meng, X.; Wang, Q.; Zhang, R.; Han, P.; Han, Kl.; Chen, J.; et al. Highly Luminescent One-Dimensional Organic−Inorganic Hybrid Double-Perovskite-Inspired Materials for Single-Component Warm White-Light-Emitting Diodes. *Angew. Chem., Int. Ed.* **2022**, *62* (2), No. e202213240, DOI: 10.1002/anie.202213240.

(29) Han, S.; Li, M.; Liu, Y.; Guo, W.; Hong, M.-C.; Sun, Z.; Luo, J. Tailoring of a visible-light-absorbing biaxial ferroelectric towards broadband self-driven photodetection. *Nat. Commun.* **2021**, *12* (1), No. 284.

(30) Mao, L.; Guo, P.; Kepenekian, M.; Hadar, I.; Katan, C.; Even, J.; Schaller, R. D.; Stoumpos, C. C.; Kanatzidis, M. G. Structural Diversity in White-Light-Emitting Hybrid Lead Bromide Perovskites. *J. Am. Chem. Soc.* **2018**, *140* (40), 13078−13088.

(31) Vishnoi, P.; Zuo, J. L.; Li, X.; Binwal, D. C.; Wyckoff, K. E.; Mao, L.; Kautzsch, L.; Wu, G.; Wilson, S. D.; Kanatzidis, M. G.; et al. Hybrid Layered Double Perovskite Halides of Transition Metals. *J. Am. Chem. Soc.* **2022**, *144* (15), 6661−6666.

(32) Zhang, Y.; Liu, X.; Sun, H.; Zhang, J.; Gao, X.; Yang, C.; Li, Q.; Jiang, H.; Wang, J.; Xu, D. Strong Self-Trapped Exciton Emissions in Two-Dimensional Na-In Halide Perovskites Triggered by Antimony Doping. *Angew. Chem., Int. Ed.* **2021**, *60* (14), 7587−7592.

(33) Li, B.; Jin, J.; Yin, M.; Zhang, X.; Molokeev, M. S.; Xia, Z.; Xu, Y. Sequential and Reversible Phase Transformations in Zero-Dimensional Organic-Inorganic Hybrid Sb-based Halides towards Multiple Emissions. *Angew. Chem., Int. Ed.* **2022**, *61* (49), No. e202212741.

(34) Mo, Q.; Yu, J.; Chen, C.; Cai, W.; Zhao, S.; Li, H.; Zang, Z. Highly Efficient and Ultra-Broadband Yellow Emission of Lead-Free Antimony Halide toward White Light-Emitting Diodes and Visible Light Communication. *Laser Photonics Rev.* **2022**, *16* (10), No. 2100600.

(35) Shi, C.; Ye, L.; Gong, Z.-X.; Ma, J.-J.; Wang, Q.-W.; Jiang, J.-Y.; Hua, M.-M.; Wang, C.-F.; Yu, H.; Zhang, Y.; et al. Two-Dimensional Organic−Inorganic Hybrid Rare-Earth Double Perovskite Ferro-electrics. *J. Am. Chem. Soc.* **2020**, *142* (1), 545−551.

(36) Vargas, B.; Rodríguez-López, G.; Solis-Ibarra, D. The Emergence of Halide Layered Double Perovskites. *ACS Energy Lett.* **2020**, *5* (11), 3591−3608.

(37) Connor, B. A.; Leppert, L.; Smith, M. D.; Neaton, J. B.; Karunadasa, H. I. Layered Halide Double Perovskites: Dimensional Reduction of $Cs_2AgBiBr_6$. *J. Am. Chem. Soc.* **2018**, *140* (15), 5235−5240.

(38) Tran, T. T.; Quintero, M. A.; Arpino, K. E.; Kelly, Z. A.; Panella, J. R.; Wang, X.; McQueen, T. M. Chemically controlled crystal growth of $(CH_3NH_3)_2AgInBr_6$. *CrystEngComm* **2018**, *20* (39), 5929−5934.

(39) Dolomanov, O. V.; Bourhis, L. J.; Gildea, R. J.; Howard, J. A. K.; Puschmann, H. OLEX2: a complete structure solution, refinement and analysis program. *J. Appl. Crystallogr.* **2009**, *42* (2), 339−341.

(40) Zhou, J.; Xie, P.; Wang, C.; Bian, T.; Chen, J.; Liu, Y.; Guo, Z.; Chen, C.; Pan, X.; Luo, M.; et al. Hybrid Double Perovskite Derived Halides Based on Bi and Alkali Metals (K, Rb): Diverse Structures, Tunable Optical Properties and Second Harmonic Generation Responses. *Angew. Chem., Int. Ed.* **2023**, *62*, No. e202307646, DOI: 10.1002/anie.202307646.

(41) Chen, D.; Hao, S.; Fan, L.; Guo, Y.; Yao, J.; Wolverton, C.; Kanatzidis, M. G.; Zhao, J.; Liu, Q. Broad Photoluminescence and Second-Harmonic Generation in the Noncentrosymmetric Organic−Inorganic Hybrid Halide $(C_6H_5(CH_2)_4NH_3)_4MX_7 \cdot H_2O$ (M = Bi, In, X = Br or I). *Chem. Mater.* **2021**, *33* (20), 8106−8111.

(42) Chen, D.; Hao, S.; Zhou, G.; Deng, C.; Liu, Q.; Ma, S.; Wolverton, C.; Zhao, J.; Xia, Z. Lead-Free Broadband Orange-Emitting Zero-Dimensional Hybrid $(PMA)_3InBr_6$ with Direct Band Gap. *Inorg. Chem.* **2019**, *58* (22), 15602−15609.

(43) Pandey, S.; Nair, A.; Andrews, A. P.; Venugopal, A. 2,6-Diisopropylanilinium Bromobismuthates. *Eur. J. Inorg. Chem.* **2017**, *2017* (4), 798−804.

(44) Li, D.-Y.; Sun, Y.-M.; Xu, Z.-Y.; Xiao, P.-C.; Song, J.-H.; Lei, X.-W.; Chen, G.; Yue, C.-Y. 0D hybrid indium halides with highly efficient intrinsic broadband light emissions. *Chem. Commun.* **2022**, *58* (65), 9084−9087.

(45) Saparov, B.; Mitzi, D. B. Organic−Inorganic Perovskites: Structural Versatility for Functional Materials Design. *Chem. Rev.* **2016**, *116* (7), 4558−4596.

(46) Zhou, L.; Liao, J. F.; Huang, Z. G.; Wei, J. H.; Wang, X. D.; Li, W. G.; Chen, H. Y.; Kuang, D. B.; Su, C. Y. A Highly Red-Emissive Lead-Free Indium-Based Perovskite Single Crystal for Sensitive Water Detection. *Angew. Chem., Int. Ed.* **2019**, *58* (16), 5277−5281.

(47) Li, Z.; Li, Y.; Liang, P.; Zhou, T.; Wang, L.; Xie, R.-J. Dual-Band Luminescent Lead-Free Antimony Chloride Halides with Near-Unity Photoluminescence Quantum Efficiency. *Chem. Mater.* **2019**, *31* (22), 9363−9371.

(48) Noculak, A.; Morad, V.; McCall, K. M.; Yakunin, S.; Shynkarenko, Y.; Wörle, M.; Kovalenko, M. V. Bright Blue and Green Luminescence of Sb(III) in Double Perovskite Cs_2MInCl_6 (M = Na, K) Matrices. *Chem. Mater.* **2020**, *32* (12), 5118−5124.

(49) McCall, K. M.; Stoumpos, C. C.; Kostina, S. S.; Kanatzidis, M. G.; Wessels, B. W. Strong Electron−Phonon Coupling and Self-Trapped Excitons in the Defect Halide Perovskites $A_3M_2I_9$ (A = Cs, Rb; M = Bi, Sb). *Chem. Mater.* **2017**, *29* (9), 4129−4145.